



ARTICLE

Numerical Investigation of Stress and Toughness Contrast Effects on the Vertical Propagation of Fluid-Driven Fractures in Shale Reservoirs

Manqing Qian^{*}, Xiyu Chen and Yongming Li

State Key Laboratory of Oil & Gas Reservoir Geology and Exploitation, Southwest Petroleum University, Chengdu, 610500, China

^{*}Corresponding Author: Manqing Qian. Email: qianmanqing719@163.com

Received: 29 November 2024; Accepted: 13 March 2025; Published: 30 June 2025

ABSTRACT: Shale reservoirs are characterized by numerous geological discontinuities, such as bedding planes, and exhibit pronounced heterogeneity across rock layers separated by these planes. Bedding planes often possess distinct mechanical properties compared to the surrounding rock matrix, particularly in terms of damage and fracture behavior. Consequently, vertical propagation of hydraulic fractures is influenced by both bedding planes and the heterogeneity. In this study, a numerical investigation into the height growth of hydraulic fractures was conducted using the finite element method, incorporating zero-thickness cohesive elements. The analysis explored the effects of bedding planes, toughness contrasts between layers, and variations in *in-situ* stress across different strata. The results reveal that hydraulic fractures are more likely to propagate along bedding planes instead of traversing them and extending vertically into barrier layers when (1) bedding strength is low, (2) stress contrast between layers is high, and (3) toughness contrast is significant. Furthermore, for a given bedding strength, increased stress contrast or higher toughness contrast between layers elevate hydraulic fracture extension pressure. When a substantial stress difference exists between layers ($L_c = 0.4$), hydraulic fractures preferentially propagate along bedding planes. Conversely, as bedding strength increases, the propagation distance along bedding planes decreases, accompanied by an amplified horizontal compressive stress field. Notably, when the stress difference is sufficiently small ($SD < -0.2$), a phenomenon termed “stress rolling” emerges, wherein hydraulic fractures deviate from vertical growth and instead extend along a near-horizontal trajectory.

KEYWORDS: Fluid-driven fracture; hydraulic fracturing; fracture height growth; cohesive element; bedding planes

1 Introduction

Shale reservoirs, typically deeply buried, exhibit low porosity and permeability due to their compact pore structure. These inherent properties necessitate advanced stimulation techniques to enable efficient hydrocarbon extraction. Among these, hydraulic fracturing plays a critical role by generating artificial fracture networks to enhance reservoir productivity.

Controlling hydraulic fracture height remains crucial for ensuring successful fracturing operations. Inaccurate fracture height predictions may compromise optimized fracturing designs, potentially causing fluid and proppant migration into non-productive zones or aquifer penetration, which risks undesired fluid influx. For decades, researchers have widely recognized the stress contrast between geological layers as the primary factor influencing hydraulic fracture height growth. However, models relying solely on stress contrast tend to overpredict fracture heights compared with field observations [1–3]. This discrepancy is attributed to the neglect of the influence of geological discontinuities (e.g., bedding planes) in existing models. These structural features exhibit distinct mechanical properties, such as fracture toughness, that



significantly differ from those of the intact rock matrix. Consequently, bedding planes can disturb hydraulic fracture propagation [4].

The effectiveness of bedding planes in restricting fracture height growth primarily depends on their intrinsic properties, including interfacial strength, dip angle, and bedding plane density (defined as the number of planes per unit interval). Early laboratory experiments showed that uncemented or weakly cemented bedding planes typically arrest hydraulic fracture propagation [5]. Through combined theoretical and experimental analyses, Daneshy identified the strength of bedding planes between adjacent layers as a key factor in influencing fracture height growth. When interfacial bonding between layers is strong, fractures are difficult to contain within the reservoir, whereas weak interfaces effectively limit fracture height [6]. Xu et al. examined the role of interface density in fracture containment. Their results indicated that a single interface acts as a toughness or stiffness barrier, while multiple closely spaced interfaces collectively form a stress barrier. The effectiveness of interfaces to constrain fracture height improves with increased bedding plane density [7]. Huang et al. employed the Cohesive Zone Method (CZM) to analyze the impact of dip angle on hydraulic fracture propagation in coal-rock formations. Their findings indicated that at dip angles of 0° and 15° , hydraulic fractures (HFs) propagate along the maximum horizontal principal stress direction without substantial branching. At dip angles of 30° and 45° , HFs penetrate the bedding plane, generating branched networks with significant shear slip. As dip angles increase to 60° and 75° , HFs become confined between bedding layers [8].

Variations in rock mechanical properties, such as elastic modulus, fracture toughness, and *in-situ* stress conditions, significantly affect fracture propagation patterns in stratified formations. Gudmundsson and Brenner demonstrated that rock layers with elastic moduli 10–100 times lower than adjacent formations absorb most tensile stresses at fracture tips [9]. This stress absorption impedes vertical fracture expansion and forms T-shaped fractures, as shown in Fig. 1. Jeffrey and Bunger further emphasized that stiffness contrasts across interfaces create stress differences, effectively acting as barriers to vertical fracture growth [10]. Huang et al. investigated the effects of stiffness, toughness, and stress contrasts between layers, particularly under interfacial slip conditions. Huang's findings indicated that the elastic modulus ratio between adjacent layers primarily governs how hydraulic fractures approach interfaces. After the fracture reaches an interface, its further propagation is primarily controlled by the toughness contrast. If the fracture penetrates the interface, the stress contrast then becomes the dominant factor controlling vertical growth [11].

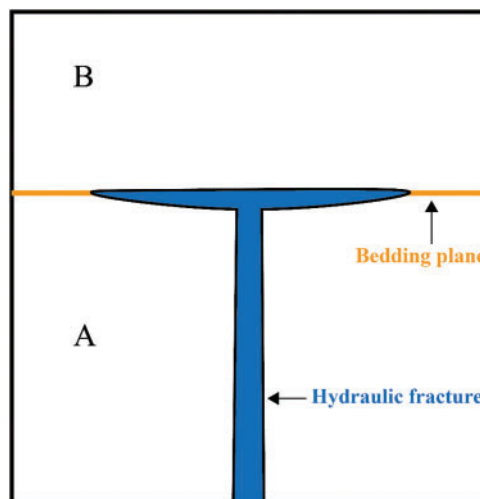


Figure 1: The T-shaped growth of hydraulic fractures

Previous studies have demonstrated that rock mechanical properties and bedding planes significantly influence fracture propagation in shale reservoirs. However, fracture height growth is influenced by multiple factors. A thorough analysis of reservoir stress state, material properties, and structural characteristics is necessary to improve prediction accuracy and optimize fracturing outcomes. Given the complexity of reservoir systems, conducting large-scale fracture propagation studies solely through laboratory experiments is prohibitively difficult. Therefore, numerical simulations, which integrate these reservoir characteristics with field data, have become widely adopted for studying fracture height growth. Several numerical methods are frequently employed, including the Discrete Element Method (DEM), the Displacement Discontinuity Method (DDM), the Extended Finite Element Method (XFEM), and the Cohesive Zone Method (CZM) are commonly applied. For example, Xie et al. employed 3D displacement discontinuity modeling to investigate the effects of shear displacement discontinuities along bedding planes on vertical fracture growth [12]. Zheng et al. applied a block-based discrete element method to analyze the influence of operational parameters, such as fluid viscosity and injection rate, on hydraulic fracture penetration through bedding planes [13]. Cong et al. developed a numerical model to simulate fracture propagation in stratified formations, incorporating *in-situ* stress, rock mechanical properties, and operational parameters [14]. Ma et al. applied XFEM and CZM to study fracture trajectories and morphology evolution under different lithological combinations and stress conditions [15]. Wang et al. utilized global cohesive zone elements to investigate fracture height growth in shale reservoirs, considering interface strength, perforation location, and injection rate [16]. Existing research suggests that the Displacement Discontinuity Method (DDM) provides efficient and accurate fracture propagation simulations. However, DDM encounters limitations when applied to heterogeneous materials such as bedding planes. XFEM enhances fracture geometry simulation accuracy by converting nodes into specialized crack-tip elements. Nevertheless, XFEM encounters difficulties in modeling complex interactions between hydraulic fractures and multilayer rock formations.

Incorporating cohesive elements into finite element meshes enables the simulation of interactions between hydraulic fractures and bedding planes. In stratified reservoirs, fracture propagation typically involves multiple coupled mechanisms rather than a single failure mode. The cohesive element method can simulate fracture propagation under various fracture modes, including tensile, shear, and mixed-mode extension.

This study employs numerical simulations using finite element meshes with zero-thickness cohesive elements to examine the combined effects of bedding planes and mechanical differences between layers on fracture height growth. The simulations specifically investigate the influence of bedding plane properties (including bedding strength and dip angle), toughness contrast (K_c), stress difference between layers (L_c), and stress difference between the vertical stress and the horizontal minimum principal stress (SD) on fracture height growth. Simulation results are illustrated through parametric diagrams, clearly depicting various fracture propagation scenarios. These findings enhance understanding of fracture height propagation mechanisms in stratified formations and provide practical insights for optimizing fracture design processes in unconventional reservoirs.

2 Governing Equation

To model the hydraulic fracturing process, the governing equations for fluid–solid coupling in porous media must include several key components: momentum balance equations describing solid (rock) deformation, continuity equations governing fluid flow within both the rock matrix and fractures, and criteria defining fracture initiation and propagation.

2.1 Momentum Balance Equations for Solid Deformation

A shale reservoir is a porous medium consisting of a rock skeleton, pore fluid, and the pore space. Shales can be modeled as multiphase materials, in which effective stress as a key parameter describing stress and pore pressure interactions. According to Biot's theory [17], the effective stress in the rock matrix can be expressed as:

$$\sigma = \bar{\sigma} + \alpha p_w \quad (1)$$

where σ is the total stress in the rock matrix, Pa; $\bar{\sigma}$ is the effective stress, Pa; p_w is the pore pressure, Pa; α is the elasticity coefficient of the rock matrix (Biot coefficient, dimensionless).

The deformation equation in the rock matrix can be derived from Eq. (1) [18]:

$$\int_V (\bar{\sigma} + p_w I) \delta_\epsilon dV = \int_S t \cdot \delta_V dS + b \cdot \delta_V dV \quad (2)$$

where I is the unit matrix; δ_ϵ is the virtual strain rate tensor, s^{-1} ; dV is the element volume, m^3 , t is the traction per unit area, N/m^2 , δ_V is the virtual velocity, m/s ; and dS is the area of the element where the surface force acts, m^2 ; b is the body force per unit volume.

2.2 Continuity Equations for Fluid Flow

(1) Fluid flow in porous rock matrix

According to mass conservation, the fluid mass entering a rock's pore space over a time interval equals the sum of the fluid stored in the pore volume and the fluid flowing out. Therefore, the continuity equation governing fluid flow in the matrix can be expressed as [19]:

$$\frac{1}{J} \frac{\partial}{\partial t} (J \rho_w n_w) + \frac{\partial}{\partial x} (\rho_w n_w v_w) = 0 \quad (3)$$

where J is the change in fluid volume within the rock matrix (dimensionless); ρ_w is the fluid density, kg/m^3 ; n_w is the void ratio, related to the porosity of the rock matrix (dimensionless); v_w is the fluid seepage velocity, m/s , x is a space vector, m .

Assuming that fluid flow in the rock pores around the fracture follows Darcy's Law, the fluid seepage velocity can be expressed as:

$$v_w = -\frac{1}{\rho_w n_w g} k \cdot (\nabla p_w - \rho_w g) \quad (4)$$

where k is the permeability coefficient of the rock matrix, m/s ; g is the gravitational acceleration, m/s^2 ; and ∇p_w is the pressure gradient along the fluid flow direction in the rock matrix.

Wherein the permeability coefficient is k :

$$k = \hat{K} \frac{\rho_w g}{\mu} \quad (5)$$

where \hat{K} is the permeability of the rock matrix, m^2 ; μ is the fracturing fluid viscosity, $Pa \cdot s$.

(2) Fluid flow within the fracture

To simplify the analysis and avoid additional complexity arising from fluid property changes during flow (such as with fracturing fluids), it is assumed that the fluid within the fracture behaves as an incompressible

Newtonian fluid. Fluid flow within an open fracture is classified into tangential and normal flow, as illustrated in Fig. 2. Tangential flow occurs in the direction of fracture propagation, and normal flow is the fluid filtration from fracture surfaces into the formation. The tangential flow can be expressed as [20]:

$$q_f = -\frac{w^3}{12\mu} \nabla p_f \quad (6)$$

where w is the fracture width, m; μ is the fracturing fluid viscosity, Pa·s; ∇p_f is the fluid pressure gradient within the fracture.

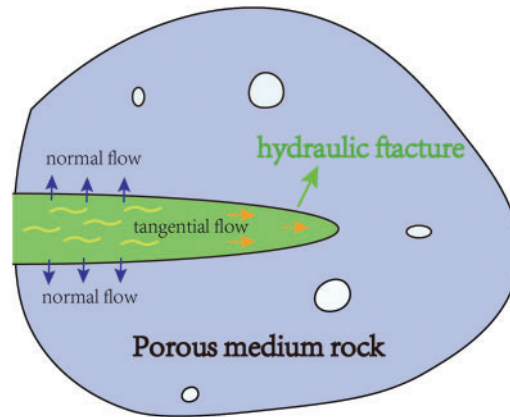


Figure 2: Fluid flow in propagating fracture

The normal flow equation is:

$$q_l = q_t + q_b \quad (7)$$

$$\begin{cases} q_t = c_t (p_f - p_t) \\ q_b = c_b (p_f - p_b) \end{cases} \quad (8)$$

where q_t and q_b represent the normal flow rates into the top and bottom surfaces of the fracture, respectively. c_t and c_b are the corresponding fluid leak-off coefficients. p_f is the fluid pressure within the fracture. p_t and p_b refer to the pore pressures at the top and bottom surfaces of the fracture, respectively.

Mass conservation within the fracture (for fluid volume) requires that the divergence of tangential flow plus the leak-off through the fracture surfaces equals the injection source. In weak form, the continuity (volume balance) for the fracture can be written including a Dirac delta for the injection point [21]:

$$\frac{\partial w}{\partial t} + \nabla q_f + q_l = Q(t) \delta(x, y) \quad (9)$$

where $Q(t)$ is the injection rate, m²/s; $\delta(x,y)$ is the Dirac delta (which is zero except at the injection location).

2.3 Fracture Initiation and Propagation Criteria

(1) Initiation criteria

In the cohesive damage theory, fracture propagation initiates at the fracture tip or within the cohesive zone when cohesive forces are overcome, leading to gradual separation. Cohesive element adopts a traction-separation model, where linear elastic behavior is assumed prior to damage initiation. This linear elastic

behavior represents the intrinsic elastic response of the material, defining the relationship between traction and separation before damage onset. Prior to damage initiation, stress and strain within the cohesive element follow a linear elastic relationship, expressed mathematically as follows:

$$t = \begin{Bmatrix} t_n \\ t_s \\ t_t \end{Bmatrix} = K \cdot \varepsilon = \begin{bmatrix} K_{nn} & K_{ns} & K_{nt} \\ K_{ns} & K_{ss} & K_{st} \\ K_{ns} & K_{st} & K_{tt} \end{bmatrix} \cdot \begin{Bmatrix} \varepsilon_n \\ \varepsilon_s \\ \varepsilon_t \end{Bmatrix} = E\varepsilon \quad (10)$$

where t represents the stress vector carried by the cohesive element, while t_n , t_s and t_t denote the stresses in the normal and two tangential directions, respectively. K denotes the elastic stiffness matrix of the cohesive element.

The maximum nominal stress damage criterion specifies that damage in a cohesive element occurs when the stress in any direction exceeds the critical threshold. The criterion for initial damage is expressed as follows:

$$\max \left\{ \frac{\langle t_n \rangle}{t_n^0}, \frac{t_s}{t_s^0}, \frac{t_t}{t_t^0} \right\} = 1 \quad (11)$$

where t_n^0 , t_s^0 and t_t^0 are the normal and two orthogonal shear components of traction on the cohesive element, and $\langle \cdot \rangle$ denotes the McCauley function, indicating no damage during pure compressive deformation or stress states.

(2) Propagation criteria

Once the material within a cohesive element meets the initial damage criterion, the damage evolution criterion describes the progression of stiffness degradation. When the material satisfies the condition outlined in Eq. (12), the element enters the damage evolution stage, during which its stiffness gradually degrades under the influence of external forces. The governing equations for this stage are given by:

$$t_n = \begin{cases} (1-D)\bar{t}_n & \bar{t}_n \geq 0 \\ \bar{t}_n & \bar{t}_n < 0 \end{cases} \quad (12)$$

$$\begin{cases} t_s = (1-D)\bar{t}_s \\ t_t = (1-D)\bar{t}_t \end{cases} \quad (13)$$

where \bar{t}_n , \bar{t}_s and \bar{t}_t are the stresses estimated under the linear elastic framework for the normal and two shear components, respectively.

The variation of the damage variable D depends on the softening properties of the material and can be either linear or exponential, based on the effective displacement (as shown in Fig. 3). It is given by:

$$D = \frac{\delta_m^f (\delta_m^{\max} - \delta_m^0)}{\delta_m^{\max} (\delta_m^f - \delta_m^0)} \quad (14)$$

where δ_m^f is the effective displacement at complete damage, δ_m^0 is the effective displacement at initial damage, and δ_m^{\max} is the maximum effective displacement during loading.

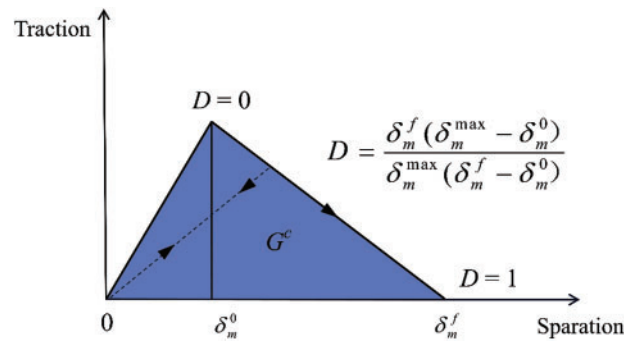


Figure 3: Cohesive traction-separation law

3 Model Validation and Numerical Example Setting

3.1 Embedding Process of the Cohesive Element

The fracture tip region is influenced by the mechanical behavior of the rock and pore pressure. To simulate the growth of fracture height, a cohesive element incorporating pore pressure degrees of freedom is introduced. This element is defined as a 6-node quadrilateral, with displacement degrees of freedom at the four corner nodes (nodes 1, 2, 3, and 4) and pore pressure degrees of freedom at the two middle nodes (nodes 5 and 6), as shown in Fig. 4.

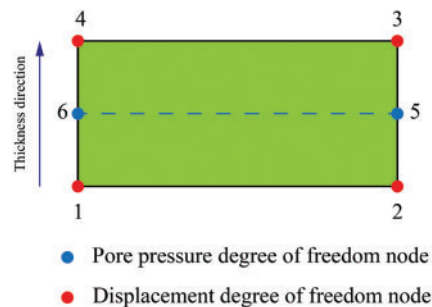


Figure 4: Cohesive elements with pore pressure nodes

The process of embedding the cohesive element into the finite element mesh involves three main steps: mesh processing, insertion of the cohesive element, and node merging, as shown in Fig. 5. The first step is to preprocess the global finite element mesh nodes (parent nodes) in the target area. Based on the mesh topology, the node numbers are updated to ensure the new sub-nodes remain independent. This step creates the interface needed to embed the cohesive element. Next, additional pore pressure nodes are inserted between the sub-nodes at the interface. Following the counterclockwise numbering principle, the independent sub-nodes are connected to the pore pressure nodes to form new interface elements. These interface elements are then aligned along the direction of the pore pressure nodes to form virtual double-node line elements, completing the embedding of the cohesive element. Finally, at the intersections of the cohesive elements in different directions, the pore pressure nodes are merged using a shared node method, ensuring fluid continuity throughout the region.

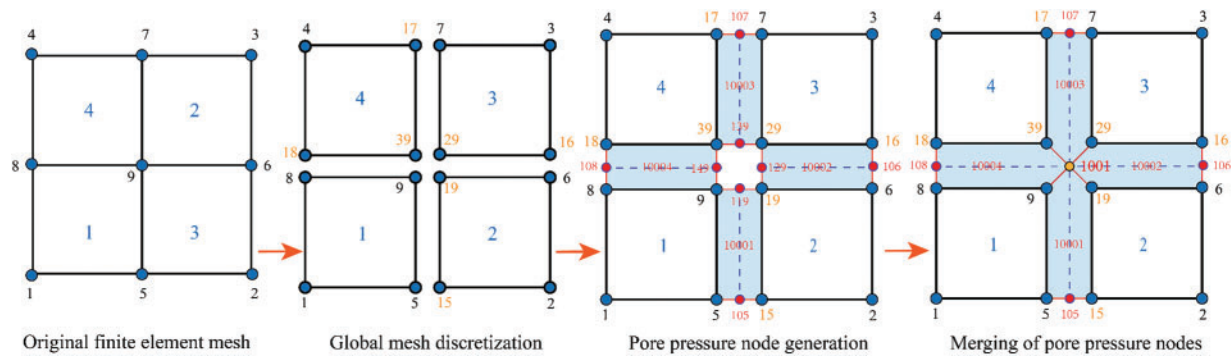


Figure 5: The process of embedding the zero-thickness cohesive element

3.2 Validation of the Numerical Model

In the absence of fluid leak-off, hydraulic fracture propagation involves two primary energy dissipation regimes: viscous-dominated and toughness-dominated. In the viscous-dominated regime, energy dissipation primarily results from the fracturing fluid flow. In the toughness-dominated regime, energy dissipation mainly arises from rock fracture and the creation of new fracture surfaces. Under plane strain conditions, these regimes can be distinguished using a dimensionless toughness parameter κ [22,23]:

$$\kappa = \frac{K'_{IC}}{(E'^3 \mu' Q)^{\frac{1}{4}}} \quad (15)$$

where K_{IC} is the Mode I fracture toughness, $K'_{IC} = 4\sqrt{\pi/2}K_{IC}$; E is the Young's modulus, $E' = E/(1 - \nu^2)$, Pa; ν is the Poisson's ratio; μ is the fluid viscosity, $\mu' = 12\mu$ Pa·s; and Q is the injection rate, m^2/s . For $\kappa < 1$, the viscous regime dominates; and when $\kappa > 4$, the toughness regime dominates. The approximate solutions for the width and length of the hydraulic fracture in the toughness-dominated regime can be expressed as follows [24]:

$$w(\xi, t) = 0.6828 \left(\frac{K'_{IC} Q t}{E'^2} \right)^{\frac{1}{3}} (1 - \xi^2)^{\frac{1}{2}} \quad (16)$$

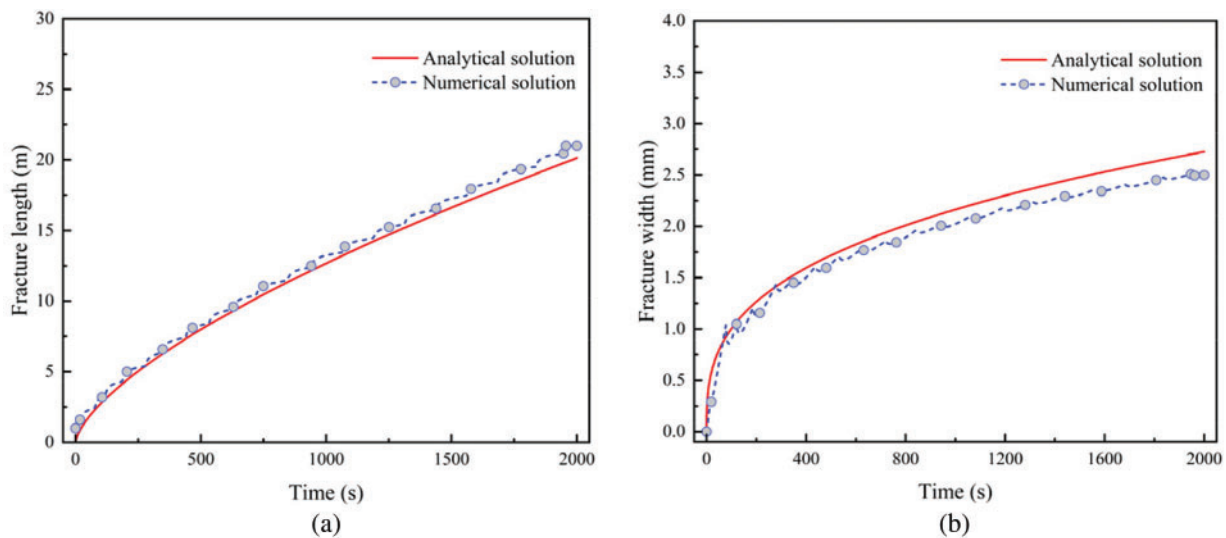
$$l(t) = 0.9324 \left(\frac{E' Q^3 t}{K'_{IC}} \right)^{\frac{2}{3}} \quad (17)$$

where w is fracture width; x represents the distance from the injection point; l is the fracture length; and t is the injection time; The normalized coordinate along the fracture width is given by $\xi = x/l$. Specific parameters used for model validation are provided in Table 1.

Using these inputs, our simulation produced fracture lengths and widths over time. Fig. 6 compares the numerical results (fracture length and width as functions of time) with the analytical KGD solution for a toughness-dominated fracture. Two main factors contribute to the minor discrepancies between the numerical and analytical solutions: (1) The analytical solution assumes an infinite domain, whereas the numerical solution is computed within a finite range. (2) The KGD model assumes the medium is impermeable; however, absolute impermeability cannot be fully realized in the numerical simulations using cohesive elements.

Table 1: Basic parameters of KGD hydraulic fracturing validation models

Parameters	Values	Unit
Young's modulus	30	GPa
Poisson's ratio	0.25	/
Injection rate (2D)	0.00002	m ² /s
Fluid viscosity	0.001	Pa·s
Injection time of duration	2000	s
Fracture toughness	4	MPa·m ^{1/2}
Dimensionless toughness	7.62	

**Figure 6:** Comparison of numerical and analytical KGD solutions: (a) hydraulic fracture length and (b) hydraulic fracture width at fracture inlet

3.3 Model Setup

Before establishing the numerical model, it is essential to validate the mesh size to ensure a suitable balance between computational accuracy and efficiency. In this study, three different mesh sizes were tested: 0.25, 0.5, and 1 m. As shown in Fig. 7, the injection pressure curve fluctuated significantly with a grid size of 1 m, indicating lower computational accuracy. Conversely, decreasing the grid size to 0.25 m improved calculation accuracy but substantially increased computational time. Thus, after carefully balancing precision and efficiency, a grid size of 0.5 m was selected for subsequent simulations.

Reservoir fracturing operations commonly encounter bedding planes with low dip angles (0° – 30°), which has prompted extensive research. However, more complex geological structures featuring high bedding dip angles (60° – 85°) frequently occur in regions such as Xinjiang's Tarim and Junggar Basins [25,26]. Given this context, this study specifically examines fracture height growth at formation dip angles of 30° and 75° , as illustrated in Fig. 8. The numerical model employed is a 2D plane strain configuration measuring $50\text{ m} \times 50\text{ m}$, divided into three distinct regions: upper and lower barrier layers, with the central section representing the reservoir. The injection point is positioned at the model's center, maintaining an equal vertical distance of 10 m from both the upper and lower bedding planes. This setup ensures the hydraulic

fracture encounters the bedding planes at consistent vertical distances for both dip angles. In the model, the minimum horizontal principal stress is oriented along the X -axis, while the vertical stress is aligned along the Y -axis. Initially, a geostatic equilibrium period of 1 s is implemented to stabilize the geo-stress and pore pressure before fracturing simulations commence. Fracturing fluid injection continues for 30 s, with an initial fracture width set at 0.002 m. The key parameters employed in the numerical model are summarized in Table 2. To maintain the comparability of simulation results, injection conditions remain consistent across all scenarios. During the parametric analysis examining fracture toughness contrast (K_c), stress differences between layers (L_c), and stress differences between the vertical stress and the horizontal minimum principal stress (SD), only the parameter under investigation is varied; all other parameters are held constant.

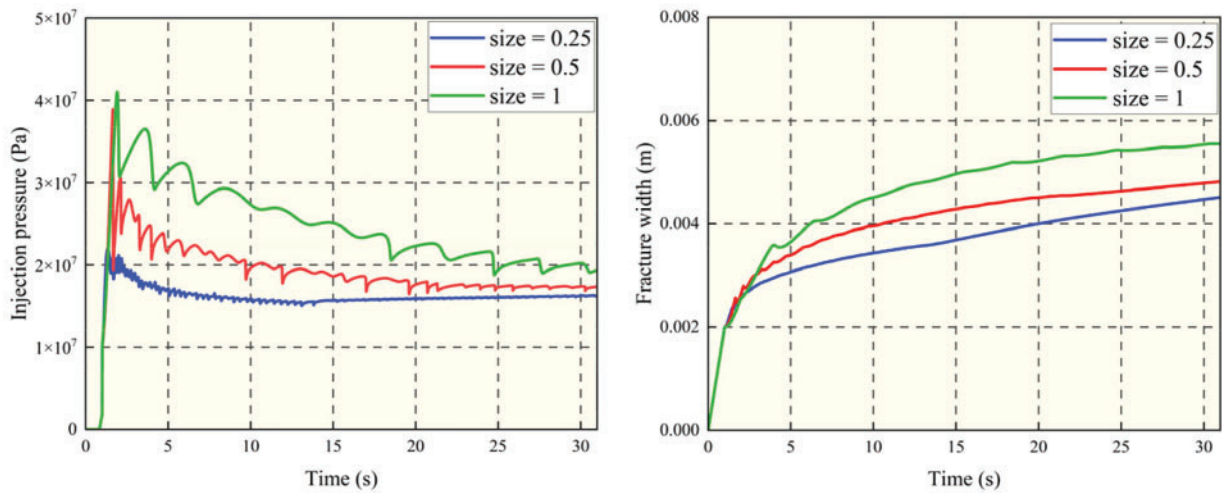


Figure 7: Mesh independence validation of injection pressure and fracture width

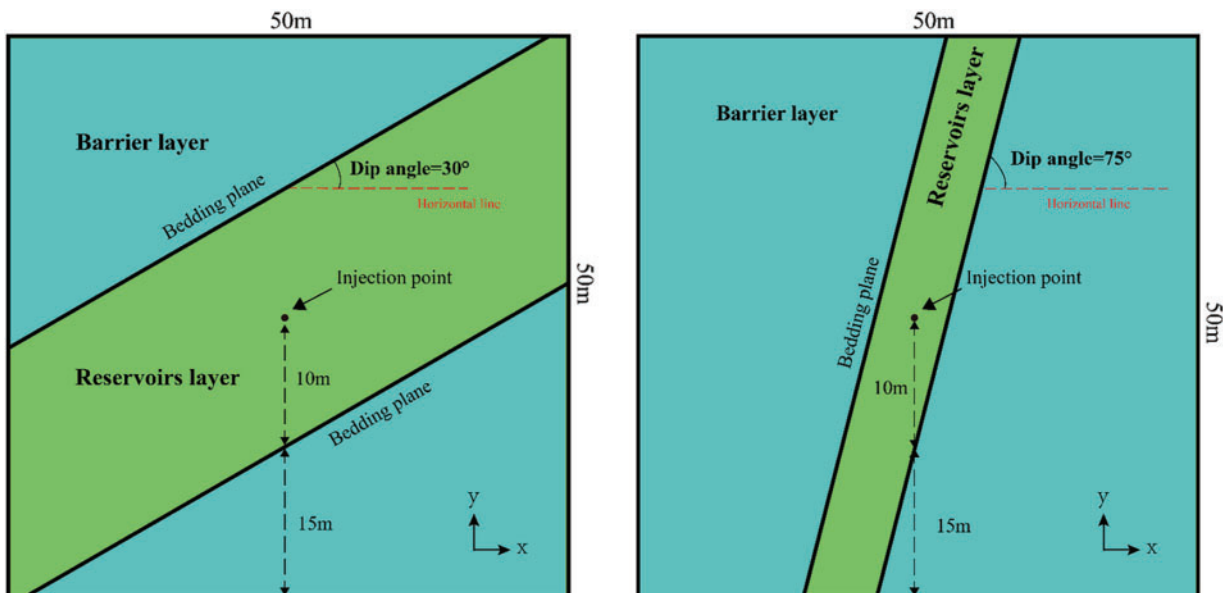


Figure 8: Numerical model setup and geometry

Table 2: Basic parameters of numerical models

Parameters		Values	Unit
Young's modulus		30	GPa
Poisson's ratio		0.25	/
Rock	Tensile strength	4	MPa
	Shear strength	20	MPa
Bedding planes	Tensile strength	1.4	MPa
	Shear strength	7	MPa
Dip angle of bedding planes		30/75	Degree
Injection rate (2D)		0.002	m ² /s
Fluid viscosity		0.001	Pa·s
Injection time of duration		30	s
Permeability		1e−7	m ²
Porosity		0.1	/
Leak-off coefficient		1e−14	m/Pa·s
Vertical stress		12	MPa
Maximum horizontal principal stress		15	MPa
Minimum horizontal principal stress		10	MPa

4 Numerical Analysis

To quantify the impact of rock mechanics parameters on fracture height growth, these parameters were expressed in dimensionless forms. The parameters include the bedding shear strength (B_s), the bedding tensile strength (B_t), the toughness contrast between layers (K_c), the stress difference between layers (L_c), and the stress difference (SD). The bedding shear strength coefficient (B_s) is defined as the ratio of shear strength between the bedding plane and the rock matrix. Similarly, the bedding tensile strength coefficient (B_t) represents the tensile strength ratio between the bedding plane and the rock matrix. The toughness contrast between layers (K_c) is defined as the ratio of fracture toughness between the reservoir and barrier layers.

The stress difference between layers L_c is defined as:

$$L_c = (\sigma_b - \sigma_R) / \sigma_R \quad (18)$$

where σ_b is the minimum horizontal principal stress of the barrier layer, MPa; and σ_R is the minimum horizontal principal stress of the reservoir layer, MPa.

Vertical to minimum horizontal stress difference SD is defined as:

$$SD = (\sigma_V - \sigma_{\min}) / \sigma_{\min} \quad (19)$$

where σ_V is the vertical stress, MPa; and σ_{\min} is the minimum horizontal principal stress, MPa.

Under different stress conditions and bedding dip angles, the fracture mode on bedding planes may vary. Under the influence of vertical stress, at lower dip angles, such as 30°, the shear stress acting on the bedding planes increases, leading to shear failure. In contrast, at higher dip angles, such as 75°, the formation tends to align with the vertical stress direction, increasing the tensile stress on the bedding planes and causing tensile failure. Therefore, this study specifically investigates how shear strength and tensile strength affect the vertical propagation of hydraulic fractures under these conditions. The key parameters used for numerical

simulations are listed in Tables 3 and 4. Additional relevant parameters are provided in Table 2. In this study, interactions between hydraulic fractures and bedding planes are classified as either traversal or diversion. Traversal refers to situations where hydraulic fractures penetrate through bedding planes, whereas diversion describes cases where hydraulic fractures propagate along bedding planes. These behaviors are illustrated in Fig. 9.

Table 3: Key parameter setting for the case of low dip angle (30°)

Parameters		Values					Unit
Dip angle		30					Degree
Shear strength of bedding plane	5	6	7	8	9		MPa
Shear strength of rock		20					MPa
B_s		0.25	0.30	0.35	0.40	0.45	/
Tensile strength of bedding plane		1.4					MPa
Tensile strength of rock		4					MPa
B_t		0.35					/

Table 4: Key parameter setting for the case of high dip angle (75°)

Parameters		Values					Unit
Dip angle		75					Degree
Shear strength of bedding plane		7					MPa
Shear strength of rock		20					MPa
B_s		0.35					/
Tensile strength of bedding plane		0.8	1.6	2.4	3.2	4	MPa
Tensile strength of rock		4					MPa
B_t		0.2	0.4	0.6	0.8	1	/

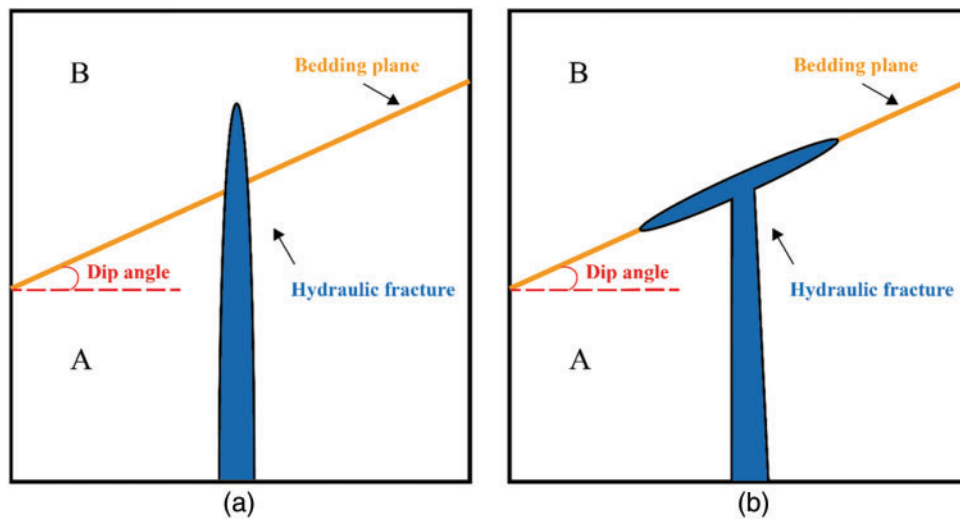


Figure 9: Fracture traversal and diversion behavior: (a) traversal; (b) diversion

4.1 Influence of Stress Difference between Layers on Height Growth

To examine the impact of stress difference between layers (L_c) on hydraulic fracture height growth, we tested L_c values of -0.4 , -0.2 , 0 , 0.2 , and 0.4 . Correspondingly, the minimum horizontal principal stress of the barrier layer was set to 6, 8, 10, 12, and 14 MPa (Table 5). All other parameters are shown in Table 2.

Table 5: Key parameters under different stress difference between layers and shear strength ratio

Parameters		Values					Unit
Dip angle		30/75					Degree
Minimum horizontal principal stress of the reservoir		10					MPa
Minimum horizontal principal stress of barrier layer		6	8	10	12	14	MPa
L_c		-0.4	-0.2	0	0.2	0.4	/
B_s		0.25	0.30	0.35	0.40	0.45	/
B_t		0.2	0.4	0.6	0.8	1	/

(1) Low dip angle

At a low dip angle of 30° , the hydraulic fracture height growth is analyzed with respect to varying stress difference between layers (L_c) and shear strength ratio (B_s), as shown in Fig. 10. Higher B_s or lower L_c promote hydraulic fracture traversal through bedding planes. Elevated fluid pressure under these conditions drives vertical propagation into the barrier layer. Conversely, lower B_s or greater L_c enhance the tendency of hydraulic fractures to divert along bedding planes. The critical shear strength threshold between traversing and diversion behavior varies according to stress difference between layers. When $L_c < 0.4$, fracture propagation behavior becomes relatively insensitive to changes in stress difference between layers, making B_s the dominant factor influencing fracture height growth. However, when $L_c = 0.4$, hydraulic fractures predominantly divert along the bedding planes, primarily due to the strong barrier effect imposed by the stress field.

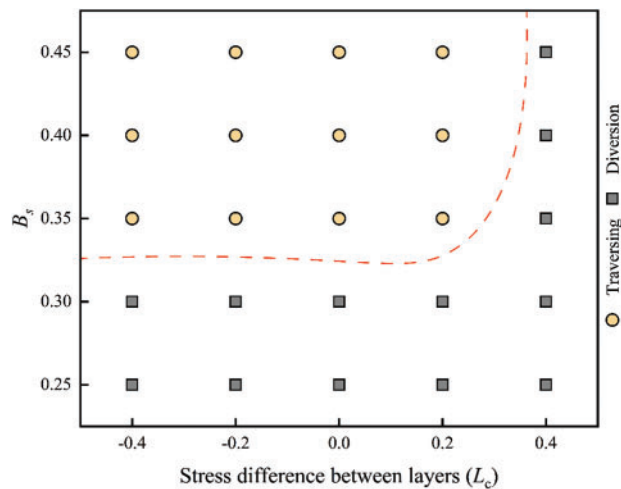


Figure 10: Numerical simulation results under the combined effect of bedding shear strength and stress difference between layers

Figs. 11 and 12 illustrate fracture morphology and stress distribution along the X-axis under different bedding shear strengths when L_c is 0.4. In these figures, PFOPEN represents the fracture width, while S and S11 represent the stress magnitude along the X-axis. The results show that as the bedding shear strength increases, the diversion distance of hydraulic fractures decreases, fracture width increases, and stress along the X-axis correspondingly rises.

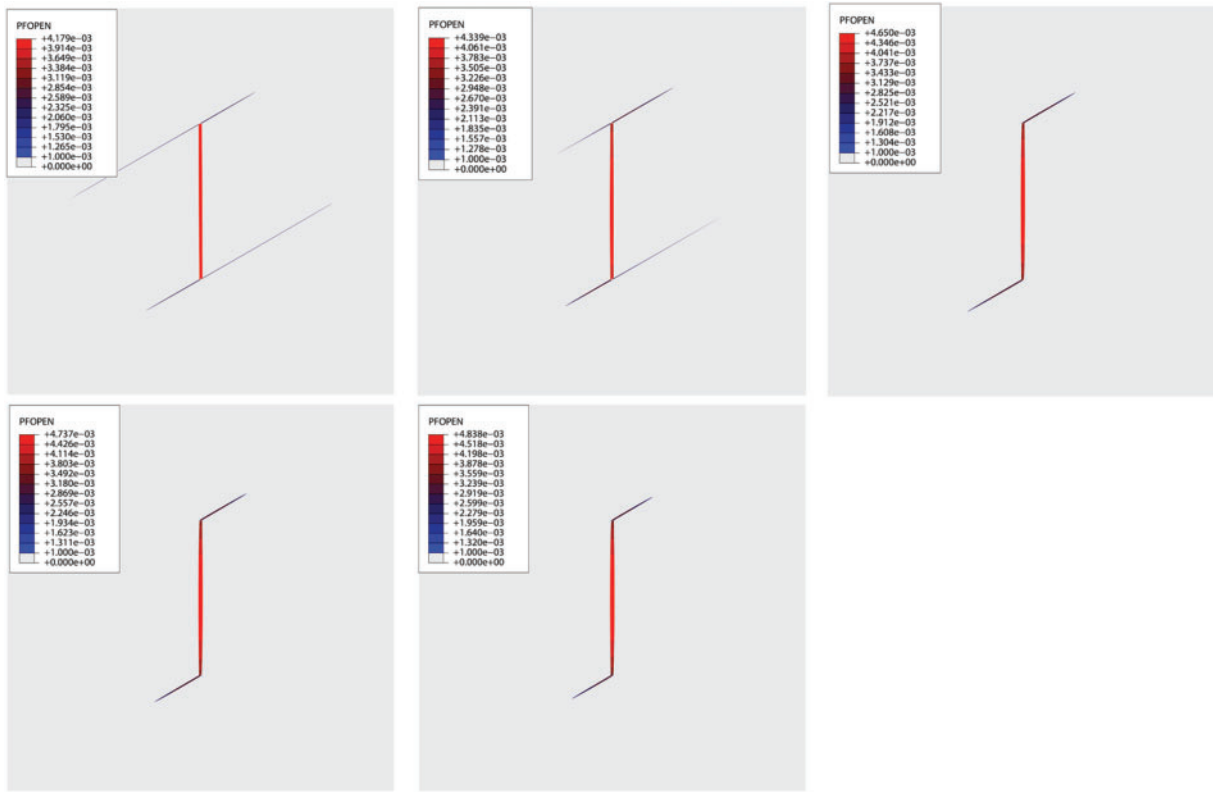


Figure 11: Fracture morphology at different bedding strength ($L_c = 0.40$)

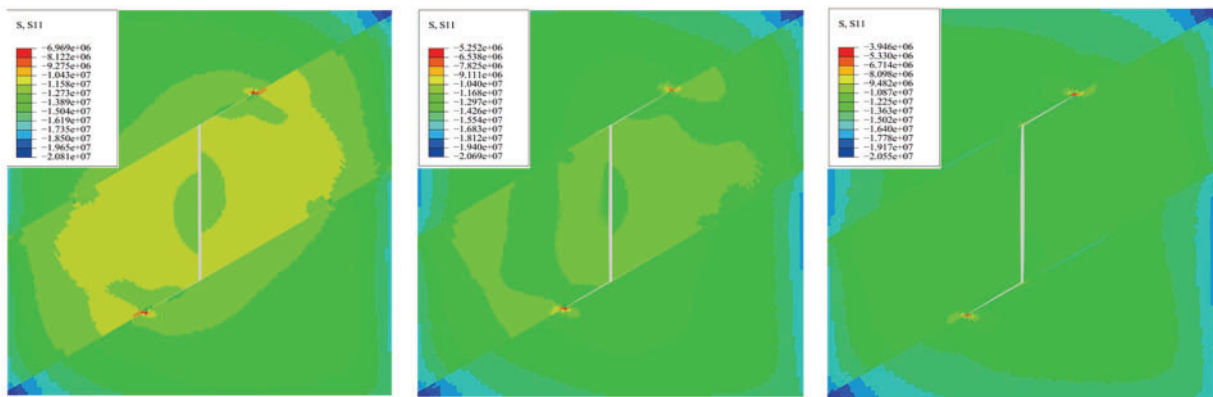


Figure 12: (Continued)

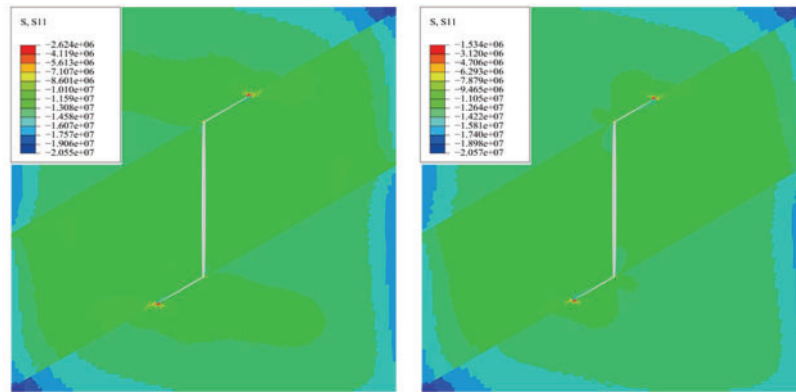


Figure 12: Stress distribution in the horizontal direction at different bedding strengths ($L_c = 0.40$)

(2) High dip angle

Fig. 13 illustrates fracture height growth at a high dip angle of 75° , considering varying L_c and B_t . The findings suggest that lower bedding plane tensile strength or larger stress difference between layers promote the diversion of hydraulic fractures along bedding planes. Furthermore, the threshold of tensile strength separating traversing and diversion behavior varies with the stress difference between layers. Unlike the scenario at low dip angles, the stress contrast between layers consistently impacts fracture propagation, regardless of whether the barrier layer exhibits higher or lower stress compared to the reservoir. When $L_c < 0$, hydraulic fractures traverse the bedding plane and propagate into the barrier layer under all examined tensile strength conditions. However, for $L_c \geq 0$, the bedding tensile strength required to prevent fracture diversion increases nearly linearly with the minimum horizontal principal stress of the barrier layer.

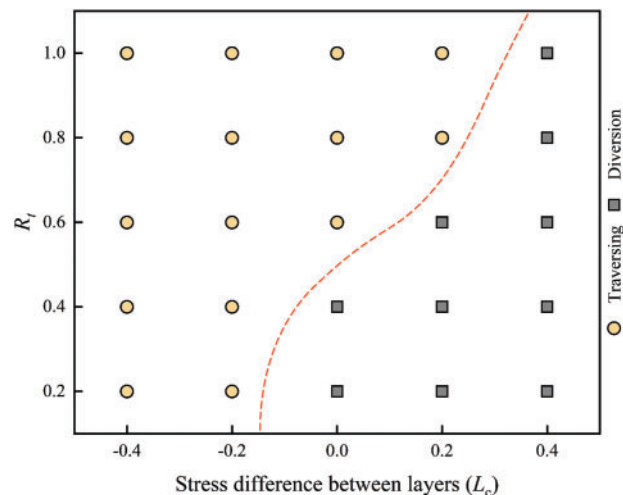


Figure 13: Numerical simulation results under the combined effect of tensile strength and stress difference between layers

For all bedding tensile strength scenarios examined, hydraulic fractures divert along bedding planes when $L_c = 0.4$, similar to the low dip angle case. This behavior indicates that stress difference between layers completely dominates fracture traversal or diversion behavior when $L_c \geq 0.4$. Under such conditions, all

hydraulic fractures divert along the bedding plane regardless of bedding strength, highlighting the significant control exerted by the high interlayer stress difference.

(3) Injection pressure and fracture width

Fig. 14 shows the injection pressure curves and fracture widths under different stress difference between layers at a tensile strength ratio of 1. The results indicate that the initiation and propagation pressures of hydraulic fractures increase with the interlayer stress difference. A larger L_c enhances the stress concentration in the adjacent barrier layers, resulting in greater compression of the reservoir layer. Consequently, this increased compression makes fracture initiation and vertical propagation more difficult. As a result, the fracture width increases, as illustrated in Fig. 14b.

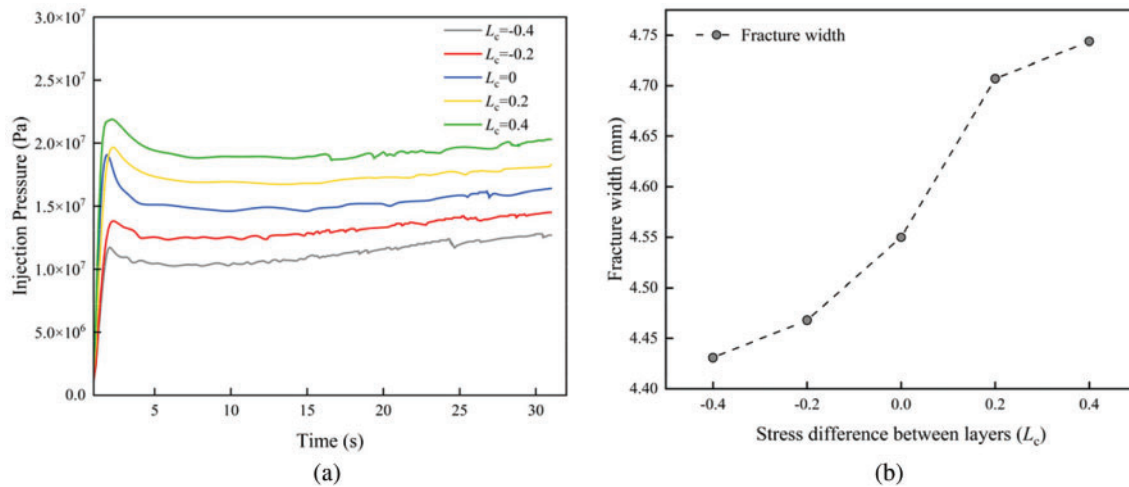


Figure 14: Injection pressure curves and fracture width at 75° dip angle ($B_t = 1$): (a) Injection pressure curves; (b) Fracture width

4.2 Influence of the Stress Difference on Height Growth

In stratified shale reservoirs, hydraulic fractures often exhibit non-planar growth patterns due to the combined effects of stress differences and bedding planes. In this study, vertical stress was varied to investigate how bedding planes influence fracture height growth under different stress conditions. The stress differences between the vertical stress and the horizontal minimum principal stress (SD) were set at -0.2 , 0 , 0.2 , 0.4 , 0.6 , and 0.8 , corresponding to vertical stress values of 8, 10, 12, 14, 16, and 18 MPa, respectively. The specific parameters are listed in Table 6, while all other parameters remain the same as those listed in Table 2.

Table 6: Key parameters under different stress difference and shear strength ratio

Parameters	Values							Unit
Dip angle	30/75							Degree
Minimum horizontal principal stress	10							MPa
Vertical stress	8	10	12	14	16	18		MPa
SD	-0.2	0	0.2	0.4	0.6	0.8		/
B_s	0.25	0.30	0.35	0.40	0.45			/
B_t	0.2	0.4	0.6	0.8	1			

(1) Low dip angle

At a low dip angle of 30° , fracture height growth was analyzed under varying SD and B_s , as shown in Fig. 15. Results indicate that lower B_s or smaller SD promote fracture propagation along the bedding planes, while higher B_s or larger SD favor hydraulic fracture traversal through the bedding planes. When $SD < 0.2$, vertical stress shows limited influence on further height growth; even with high bedding shear strength, hydraulic fractures tend to divert along the bedding plane. However, when $SD \geq 0.2$, the shear strength threshold between fracture traversal and diversion becomes independent of the stress difference, making bedding shear strength the primary controlling factor. Under such conditions, shear failure predominantly occurs along bedding planes. When a hydraulic fracture encounters a bedding plane, it propagates along the path of lower fracture energy, which is determined by shear strengths of the bedding plane and the surrounding rock matrix. For example, at low bedding shear strengths ($B_s < 0.35$), hydraulic fractures are consistently contained by the bedding plane.

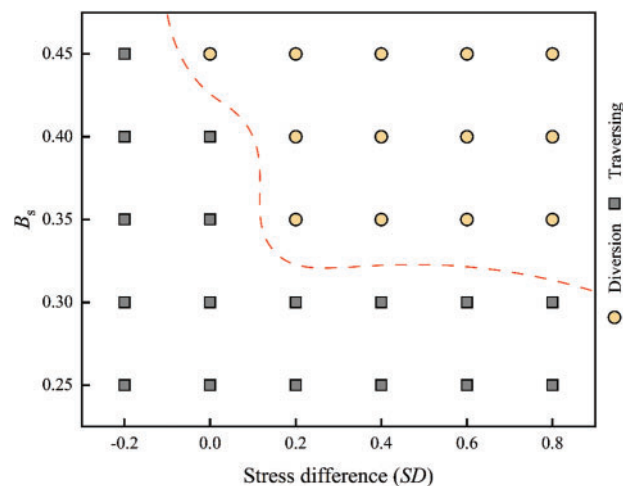


Figure 15: Numerical simulation results under the combined effect of bedding shear strength and stress difference

(2) High dip angle

Fig. 16 illustrates the growth of fracture height under different SD and B_t at a high dip angle of 75° . Results show that lower B_t or smaller SD promote hydraulic fracture diversion along bedding planes. Compared to the low dip angle scenario, hydraulic fractures at high dip angles show greater sensitivity to SD . Such sensitivity is attributed to the fact that higher stress differences promote shear failure along bedding planes. Based on the analysis in Section 4.2 (1), hydraulic fractures penetrate the bedding plane when $B_s \geq 0.35$. In this study, the bedding plane is assigned a higher shear strength ($B_s = 0.35$) under high dip angle. Therefore, at high stress differences ($SD > 0.2$), the differences in fracture behavior between low and high dip angles primarily stem from differences in B_s . When $SD \leq 0.2$, fractures divert only when the bedding tensile strength is low. This suggests that at low stress differences and high dip angles, the tensile strength of the bedding plane significantly influences fracture height growth.

Fig. 17 shows fracture morphologies under different stress differences between the vertical stress and the horizontal minimum principal stress (SD). At a low stress difference ($SD = -0.4$), hydraulic fractures propagate horizontally instead of vertically (Fig. 17a). This behavior is typical when the vertical stress is lower than the minimum horizontal principal stress—a condition often observed in shallow coal and rock layers (less than 400 m depth). With low bedding strength and small stress difference ($SD = 0$), fractures

still propagate easily along bedding planes due to reduced resistance (Fig. 17b). However, under conditions of high bedding strength and elevated horizontal stress difference ($SD = 0.4$), increased normal stress on the bedding plane enhances resistance, causing fractures to more frequently traverse the bedding plane (Fig. 17c).

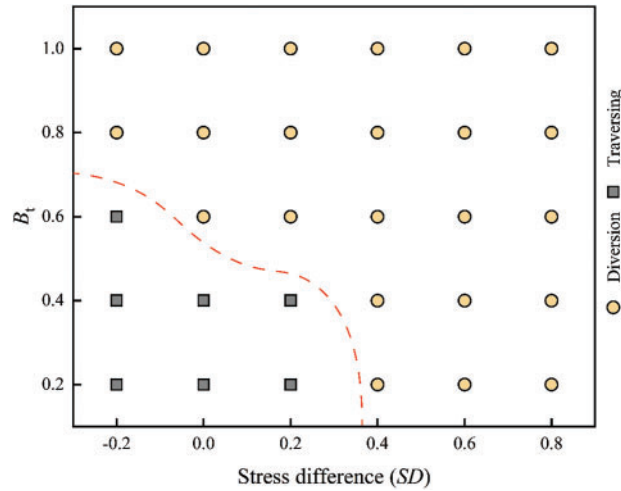


Figure 16: Numerical simulation results under the combined effect of bedding shear strength and horizontal stress difference

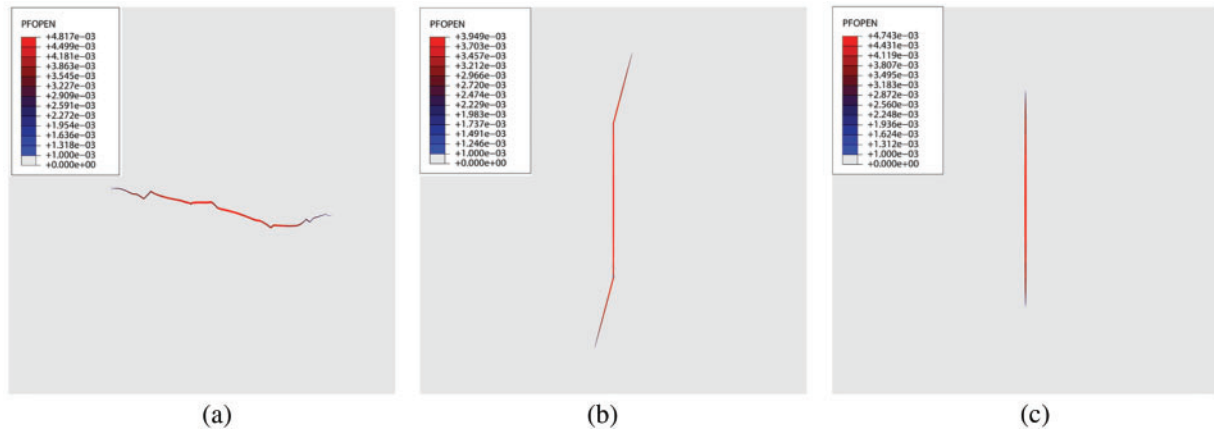


Figure 17: Fracture morphology at different horizontal stress difference: (a) $SD = -0.4$; (b) $SD = 0$; (c) $SD = 0.4$ (3) Injection pressure and fracture width

Fig. 18 shows the injection pressure curves and fracture widths under different SD when B_s is 0.45. As the stress difference increases, both the initiation and propagation pressures of hydraulic fractures rise. At higher stress differences, more energy is required to induce rock fracturing, which increases the resistance to fracture propagation. As a result, a higher net pressure is needed to overcome the high horizontal stress difference. With constant injection conditions, an increased stress difference drives the fracture to grow vertically, resulting in a reduced width.

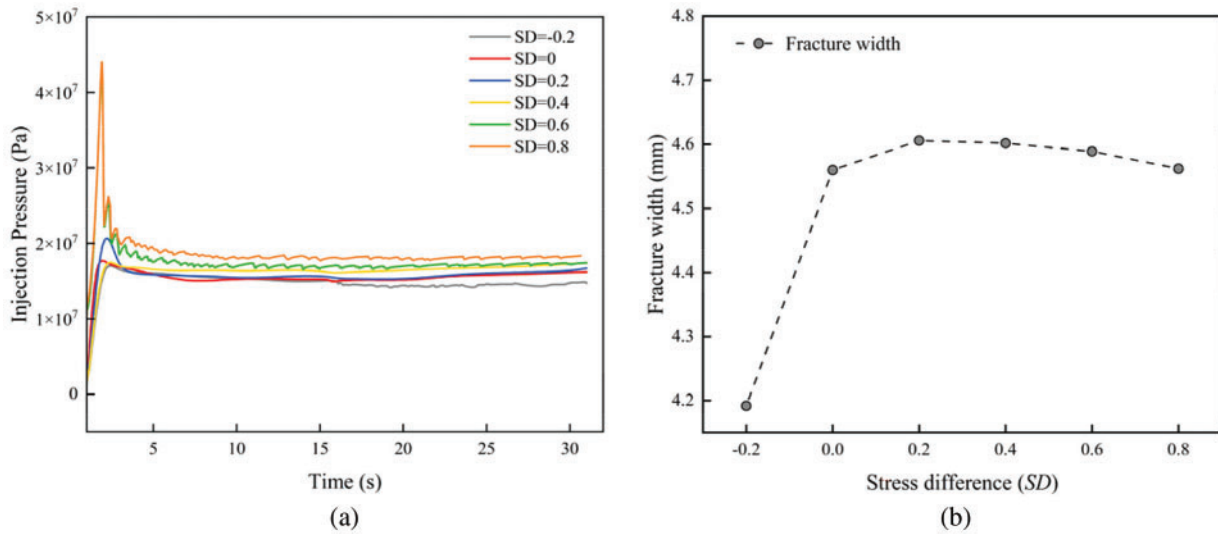


Figure 18: Injection pressure curves and fracture width at dip angle = 30° ($B_s = 0.45$): (a) Injection pressure curves; (b) Fracture width

4.3 Influence of Toughness Contrast on Height Growth

To study the effect of fracture toughness contrast between layers on hydraulic fracture height growth, the fracture toughness (K_{IC}) was assigned values of 0.5, 0.83, 1, 1.22, and 1.73. These values correspond to barrier rock matrix tensile strengths of 1, 2.8, 4, 6, and 12 MPa, respectively, as shown in Table 7. Other parameters remain the same as those in Table 2. The fracture toughness of the rock is calculated using the following equation [27]:

$$\frac{K_{IC}^2 (1 - \nu^2)}{E} = \frac{1}{2} T \delta_n \quad (20)$$

where K_{IC} is the fracture toughness, ν is Poisson's ratio, E is the elasticity modulus, T is the maximum critical stress, and δ_n is the normal displacement associated with tensile damage. Tensile damage occurs when the normal displacement reaches 0.0001 m.

Table 7: Key parameters under different toughness contrast and shear strength ratio

Parameters		Values					Unit
Dip angle		30/75					Degree
Tensile strength of the reservoir		4					MPa
Tensile strength of barrier layer		1	2.8	4	6	12	MPa
	K_c	0.5	0.7	1	1.22	1.73	/
	B_s	0.25	0.30	0.35	0.40	0.45	/
	B_t	0.2	0.4	0.6	0.8	1	

(1) Low dip angle

At a low dip angle of 30° , hydraulic fracture growth was examined under various K_c and B_s conditions, as shown in Fig. 19. The results indicate that a higher B_s or a lower K_c requires less energy for the

fluid to overcome resistance, thereby facilitating hydraulic fracture propagation across the bedding plane. Conversely, a lower B_s or a higher K_c promote the hydraulic fracture diversion along the bedding plane.

The threshold shear strength that differentiates between traversing and diversion behavior depends on the value of K_c . As K_c increases, the shear strength required to resist hydraulic fracture propagation along the bedding planes increases. When K_c is 0.5, the fracture toughness of the barrier rock ($1.27 \text{ MPa}\cdot\text{m}^{1/2}$) is comparable to that of the bedding plane ($1.49 \text{ MPa}\cdot\text{m}^{1/2}$), while the reservoir rock exhibits a significantly higher toughness of $2.52 \text{ MPa}\cdot\text{m}^{1/2}$. Under a vertical stress difference of 2 MPa ($SD = 0.2$), hydraulic fractures tend to traverse the bedding plane. However, when K_c increases to 1.73, the barrier rock's fracture toughness rises to $4.38 \text{ MPa}\cdot\text{m}^{1/2}$, while the reservoir rock's toughness remains at $2.52 \text{ MPa}\cdot\text{m}^{1/2}$. In this case, the vertical stress is insufficient to drive the fracture through the barrier layers, causing the hydraulic fracture to shear and slide along the bedding plane, which has lower fracture energy.

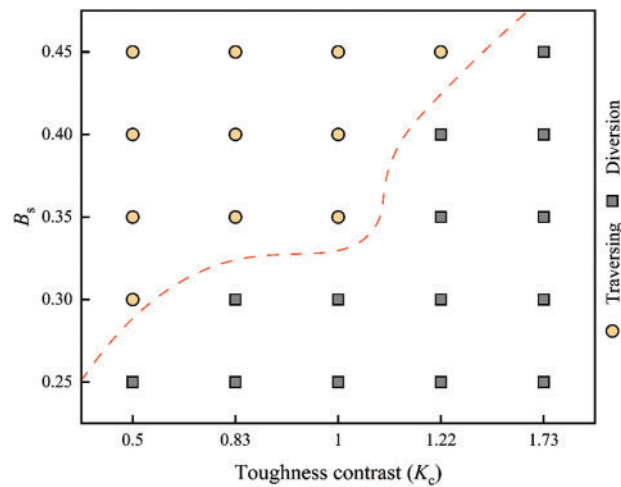


Figure 19: Numerical simulation results under the combined effect of bedding shear strength and toughness contrast

(2) High dip angle

At a high dip angle of 75° , fracture height growth under different K_c and B_t conditions is presented in Fig. 20. Similar to the low dip angle case, lower B_t or larger K_c promote the hydraulic fractures be constrained by the bedding planes. The tensile strength threshold that determines whether the fracture traverses or diverts varies with the fracture toughness contrast. When K_c is 0.5, hydraulic fractures penetrate the bedding planes and propagate into the barrier layers regardless of the bedding tensile strength. However, when K_c is 1.73, hydraulic fractures extend along the bedding plane for all tensile strength levels, indicating that fracture toughness contrast exerts a dominant effect on hydraulic fracture behavior relative to the bedding plane strength.

Fig. 21 shows the horizontal displacements (U , $U1$) for both low (30°) and high (75°) dip angles when hydraulic fractures divert under a fracture toughness contrast of 1.73 and high bedding strength ($B_s = 0.45$ or $B_t = 1$). Here, U and $U1$ represent the displacement along the x -axis. The results indicate that horizontal displacement is greater at the high dip angle compared to the low dip angle. Moreover, the propagation distance of the hydraulic fracture along the bedding plane is longer at the low dip angle. This suggests that under a high toughness contrast, more fracturing fluid leaks through low dip bedding planes, while less fluid leaks through high dip bedding planes.

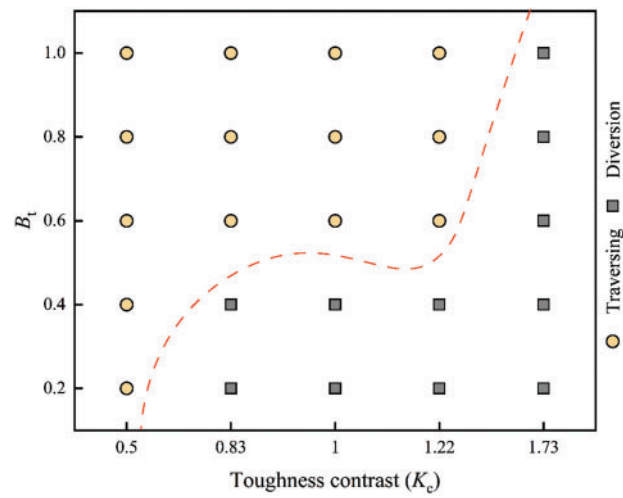


Figure 20: Numerical simulation results for the combined effect of bedding tensile strength and toughness contrast

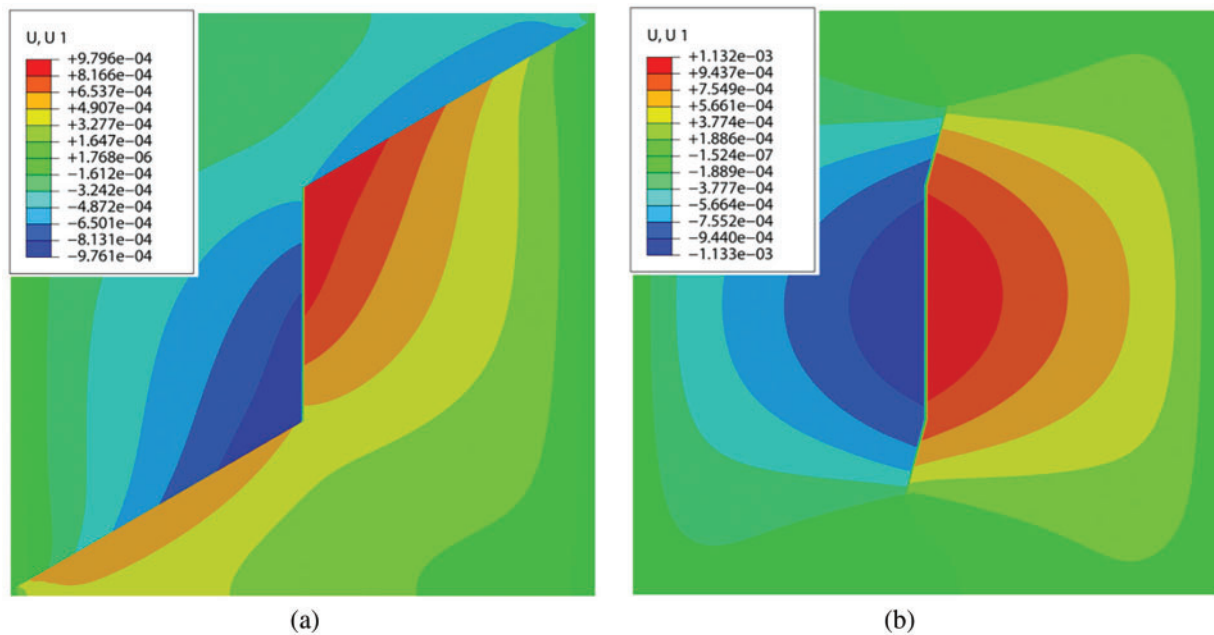


Figure 21: Horizontal displacements: (a) Low dip angle of 30°; (b) High dip angle of 75°

(3) Injection pressure and fracture width

Fig. 22 shows the injection pressure curves and fracture widths for different fracture toughness contrasts. When $K_c < 1.73$, hydraulic fractures penetrate the bedding planes. As K_c increases, the propagation pressure decreases while fracture width increases. For a high fracture toughness contrast ($K_c = 1.73$), the barrier layer exhibits significant resistance to fracture propagation. Due to the combined effect of high shear strength in the barrier layers and the high fracture toughness contrast, vertical fracture propagation is inhibited, resulting in fluid accumulation within the fracture. Once the fluid pressure exceeds the fracture pressure of the bedding plane, the fracture diverts along the bedding plane. This diversion further reduces the propagation pressure (Fig. 22a) and results in a narrower fracture width (Fig. 22b). At a fluid injection

time of 30.49 s, the hydraulic fracture nearly reaches the model boundary, as indicated by the red dashed box in Fig. 23. In the following time step, the fracture breaches the boundary, leading to significant fluid loss, a drop in pressure, and further narrowing of the fracture.

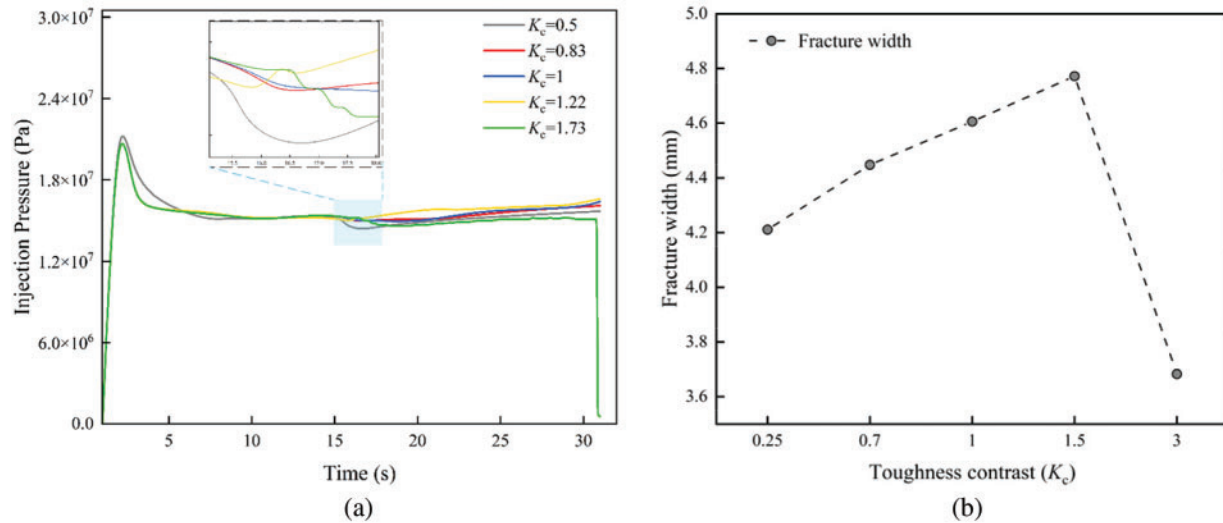


Figure 22: Injection pressure curves and fracture width at dip angle = 30° ($B_s = 0.45$): (a) Injection pressure curves; (b) Fracture width

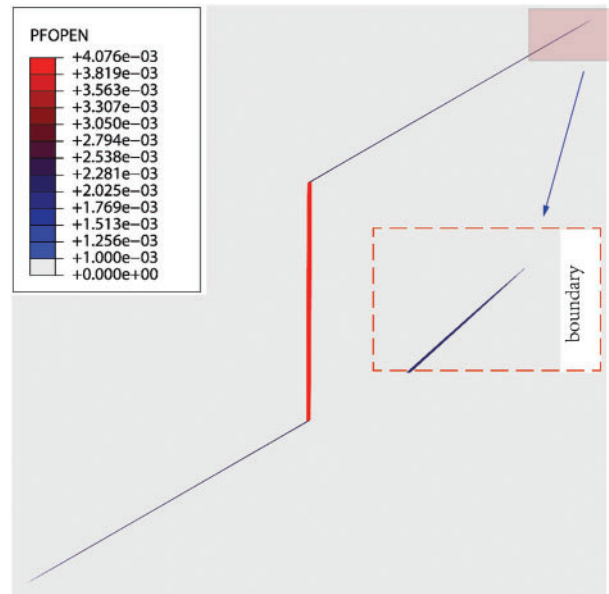


Figure 23: Fracture reaching model boundary under high toughness contrast at 30° dip angle ($K_c = 1.73$)

5 Conclusion

This study conducted numerical simulations using a finite element method with zero-thickness cohesive elements to investigate the height growth of hydraulic fractures under the combined effects of the bedding

planes (including bedding strength and dip angle), the toughness contrast (K_c), the stress difference between layers (L_c), and the stress difference between the vertical stress and the horizontal minimum principal stress (SD). The analysis focused on the behavior of hydraulic fractures as they traverse or divert based on each parameter. The key findings are as follows:

(1) Lower bedding strength, reduced stress difference (SD), higher stress difference between layers (L_c), and greater toughness contrast (K_c) promote hydraulic fracture containment within the reservoir layer. These conditions drive fractures to propagate along bedding planes rather than vertically into the barrier layers. In contrast, elevated bedding strength, increased SD , diminished L_c , and lower K_c promote vertical fracture penetration through bedding planes. Such vertical growth can be suppressed in reservoirs with weak interfacial strength and high stress/toughness barriers. In field terms, this suggests that in reservoirs with weak interfaces and high stress or toughness barriers, fractures will remain more confined in height. Optimizing injection parameters (such as injection rate and fluid viscosity) can help limit excessive height growth when such unfavorable conditions exist, thereby improving reservoir stimulation efficiency while avoiding fracture growth into unwanted layers.

(2) For a given bedding strength, increasing either the L_c or SD increases the fracture initiation and propagation pressures required. Moreover, a higher L_c leads to a wider fracture (greater width) within the reservoir, as the fracture extends laterally along the interface instead of vertically. A higher K_c similarly promotes shear slip along the bedding plane and reduces the pressure needed once the fracture diverts. In our simulations, when $K_c = 1.73$, the high toughness contrast caused the fracture to slide along the bedding plane, accompanied by a noticeable reduction in propagation pressure.

(3) When the vertical stress is sufficiently small relative to horizontal ($SD < -0.2$), hydraulic fractures did not propagate upward at all—instead, they extended laterally, essentially forming horizontal fractures. Conversely, when L_c is 0.4, fractures consistently divert along bedding planes regardless of other parameters. Stronger bedding planes shorten lateral extension distances while amplifying horizontal stress fields.

Acknowledgement: Not applicable.

Funding Statement: This research was funded by the National Natural Science Foundation of China (No. 52204052), the National Natural Science Foundation of China (No. U23B20156), and the Sichuan Science and Technology Program (No. 2023NSFSC0933).

Author Contributions: The authors confirm contribution to the paper as follows: Conceptualization, Manqing Qian and Xiyu Chen; methodology, Xiyu Chen; software, Manqing Qian; validation, Manqing Qian and Yongming Li; formal analysis, Manqing Qian; investigation, Yongming Li; resources, Xiyu Chen; data curation, Manqing Qian; writing—original draft preparation, Manqing Qian; writing—review and editing, Xiyu Chen; visualization, Manqing Qian; supervision, Yongming Li; project administration, Yongming Li; funding acquisition, Yongming Li. All authors reviewed the results and approved the final version of the manuscript.

Availability of Data and Materials: The data that support the findings of this study are available on request from the corresponding author.

Ethics Approval: Not applicable.

Conflicts of Interest: The authors declare no conflicts of interest to report regarding the present study.

Nomenclature

B_s	Bedding shear strength
B_t	Bedding tensile strength

K_c	Toughness contrast between layers
SD	Stress difference
L_c	Stress difference between layers
Q	Injection rate
E	Young's modulus
ν	Poisson's ratio
μ	Fluid viscosity
K_{IC}	The Mode I fracture toughness
κ	Dimensionless toughness
w	Fracture width at inlet
l	Fracture length

References

1. Simonson ER, Abou-Sayed AS, Clifton RJ. Containment of massive hydraulic fractures. *Soc Petrol Eng J*. 1978;18(1):27–32. doi:10.2118/6089-PA.
2. Palmer ID, Carroll HB Jr. Three-dimensional hydraulic fracture propagation in the presence of stress variations. *Soc Petrol Eng J*. 1983;23(6):870–8. doi:10.2118/10849-PA.
3. Ali Daneshy A. Factors controlling the vertical growth of hydraulic fractures. In: *SPE Hydraulic Fracturing Technology Conference*; 2009 Jan 19–21; The Woodlands, TX, USA: SPE; 2009. SPE-118789-MS. doi:10.2118/118789-ms.
4. Nie Y, Wang X, Wu B, Zhang G, Gamage RP, Li S, et al. Influences of the stress ratio and local micro mineral aggregates on small fatigue crack propagation in the shale containing bedding planes. *Int J Rock Mech Min Sci*. 2025;185(6):105980. doi:10.1016/j.ijrmms.2024.105980.
5. Rutledge J, Weng X, Yu X, Chapman C, Leane S. Bedding-plane slip as a microseismic source during hydraulic fracturing. In: *SEG Technical Program Expanded Abstracts 2016*; 2016; Dallas, TX, USA: Society of Exploration Geophysicists; 2016. p. 2555–9. doi:10.1190/segam2016-13966680.1.
6. Daneshy AA. Hydraulic fracture propagation in layered formations. *Soc Petrol Eng J*. 1978;18(1):33–41. doi:10.2118/6088-PA.
7. Xu W, Prioul R, Berard T, Weng X, Kresse O. Barriers to hydraulic fracture height growth: a new model for sliding interfaces. In: *SPE Hydraulic Fracturing Technology Conference and Exhibition*; 2019 Feb 5–7; The Woodlands, TX, USA: SPE; 2019. D011S002R005. doi:10.2118/194327-ms.
8. Huang L, Li B, Wu B, Li C, Wang J, Cai H. Study on the extension mechanism of hydraulic fractures in bed-ding coal. *Theor Appl Fract Mech*. 2024;131(3):104431. doi:10.1016/j.tafmec.2024.104431.
9. Gudmundsson A, Brenner SL. How hydrofractures become arrested. *Terra N*. 2001;13(6):456–62. doi:10.1046/j.1365-3121.2001.00380.x.
10. Jeffrey RG, Bunger A. A detailed comparison of experimental and numerical data on hydraulic fracture height growth through stress contrasts. *SPE J*. 2009;14(3):413–22. doi:10.2118/106030-PA.
11. Huang L, Dontsov E, Fu H, Lei Y, Weng D, Zhang F. Hydraulic fracture height growth in layered rocks: per-spective from DEM simulation of different propagation regimes. *Int J Solids Struct*. 2022;238(12):111395. doi:10.1016/j.ijsolstr.2021.111395.
12. Xie J, Tang J, Yong R, Fan Y, Zuo L, Chen X, et al. A 3-D hydraulic fracture propagation model applied for shale gas reservoirs with multiple bedding planes. *Eng Fract Mech*. 2020;228(2):106872. doi:10.1016/j.engfracmech.2020.106872.
13. Zheng Y, He R, Huang L, Bai Y, Wang C, Chen W, et al. Exploring the effect of engineering parameters on the penetration of hydraulic fractures through bedding planes in different propagation regimes. *Comput Geotech*. 2022;146(7):104736. doi:10.1016/j.compgeo.2022.104736.
14. Cong Z, Li Y, Tang J, Martyushev DA, Hubuqin, Yang F. Numerical simulation of hydraulic fracture height layer-through propagation based on three-dimensional lattice method. *Eng Fract Mech*. 2022;264:108331. doi:10.1016/j.engfracmech.2022.108331.

15. Ma J, Li X, Yao Q, Tan K. Numerical simulation of hydraulic fracture extension patterns at the interface of coal-measure composite rock mass with Cohesive Zone Model. *J Clean Prod.* 2023;426:139001. doi:10.1016/j.jclepro.2023.139001.
16. Wang Y, Hou B, Wang D, Jia Z. Features of fracture height propagation in cross-layer fracturing of shale oil reservoirs. *Petrol Explor Dev.* 2021;48(2):469–79. doi:10.1016/S1876-3804(21)60038-1.
17. Biot MA. General theory of three-dimensional consolidation. *J Appl Phys.* 1941;12(2):155–64. doi:10.1063/1.1712886.
18. Zienkiewicz OC, Taylor RL. The finite element method. 5th ed. London, UK: Elsevier Pte Ltd.; 2005.
19. Wang B, Zhou FJ, Wang D, Liang T, Yuan L, Hu J. Numerical simulation on near-wellbore temporary plugging and diverting during refracturing using XFEM-Based CZM. *J Nat Gas Sci Eng.* 2018;55(2):368–81. doi:10.1016/j.jngse.2018.05.009.
20. Boone TJ, Ingraffea A. A numerical procedure for simulation of hydraulically-driven fracture propagation in poroelastic media. *Int J Numer Anal Meth Geomech.* 1990;14(1):27–47. doi:10.1002/nag.1610140103.
21. Peirce A, Detournay E. An implicit level set method for modeling hydraulically driven fractures. *Comput Meth Appl Mech Eng.* 2008;197(33–40):2858–85. doi:10.1016/j.cma.2008.01.013.
22. Detournay E. Propagation regimes of fluid-driven fractures in impermeable rocks. *Int J Geomech.* 2004;4(1):35–45. doi:10.1061/(ASCE)1532-3641(2004)4:1(35).
23. Cheng S, Wu B, Zhang X, Huppert HE, Jeffrey RG. How energy dissipation mode controls the evolution of multiple plane-strain hydraulic fractures under isotropic stresses. *JGR Solid Earth.* 2024;129(8):e2024JB029179. doi:10.1029/2024JB029179.
24. Dontsov EV. An approximate solution for a plane strain hydraulic fracture that accounts for fracture toughness, fluid viscosity, and leak-off. *Int J Fract.* 2017;205(2):221–37. doi:10.1007/s10704-017-0192-4.
25. Tang S, Liu S, Tang D, Tao S, Zhang A, Pu Y, et al. Occurrence of fluids in high dip angled coal measures: geological and geochemical assessments for southern Junggar Basin. *China J Nat Gas Sci Eng.* 2021;88(4):103827. doi:10.1016/j.jngse.2021.103827.
26. Kang J, Fu X, Gao L, Liang S. Production profile characteristics of large dip angle coal reservoir and its impact on coalbed methane production: a case study on the Fukang west block, southern Junggar Basin. *China J Petrol Sci Eng.* 2018;171:99–114. doi:10.1016/j.petrol.2018.07.044.
27. Haddad M, Sepehrnoori K. XFEM-based CZM for the simulation of 3D multiple-cluster hydraulic fracturing in quasi-brittle shale formations. *Rock Mech Rock Eng.* 2016;49(12):4731–48. doi:10.1007/s00603-016-1057-2.